The transient rise of a bubble subject to shape or volume changes

B. Yang and A. Prosperetti[a)]
Department of Mechanical Engineering, The Johns Hopkins University, Baltimore, Maryland 21218

S. Takagi
Department of Mechanical Engineering, The University of Tokyo, Hongo, Bunkyo-ku, Tokyo 113, Japan

(Received 17 September 2002; accepted 23 May 2003; published 5 August 2003)

This paper deals with two problems in which the rectilinear rise of a gas bubble in a liquid undergoes a transient behavior. In the first problem, the bubble is released with a spherical, oblate, prolate, or oval shape and its evolution to steady state is simulated numerically. Contrary to some recently reported experiments, it is found that the terminal velocity and final shape are independent of the initial shape. This result suggests that the experimental observations may be influenced by uncontrolled effects rather than a genuine multivaluedness of the fluid-dynamic solution for a steadily rising bubble. The second problem concerns the ascent of a bubble which expands, or contracts, due to a change in the ambient pressure. The ensuing behavior of the rise velocity is strongly influenced by added mass effects. © *2003 American Institute of Physics.*
[DOI: 10.1063/1.1592800]

I. INTRODUCTION

It has recently been reported that the terminal velocity of a bubble rising in purified water depends on the manner in which the bubble is generated.[1,2] This unexpected experimental finding is attributed by the authors to the initial shape with which the bubble commences its ascent, which is in its turn affected by the way the bubble is generated. A bubble from a small-bore capillary executes violent shape oscillations upon its release, and is found to reach a higher steady-state velocity than a bubble of equal volume released from a wide-bore capillary, whose detachment is a much gentler process. Similar observations have also been reported independently by Tomiyama *et al.*[3,4] who, in addition to water, also experimented with silicone oils thus greatly reducing the possibility of surface contamination.

This behavior is in stark contrast with the common wisdom in the literature which, explicitly or implicitly, associates a unique rise velocity to a bubble of a given volume in a given liquid or, more generally, a unique value of the drag coefficient for given Weber and Morton numbers once the flow has become steady (see, e.g., Refs. 5 and 6).

The first case of unsteady rise studied in this paper is a numerical exploration of the effect of the initial bubble shape on its transient and, eventually, steady rise. We simulate by a boundary-fitted coordinate method bubbles sufficiently small to rise rectilinearly under normal conditions, release them with an initial spherical, prolate, oblate, or oval shape, and follow the motion until a steady state is reached. In all cases, no effect of the initial shape on the terminal velocity is found.

The second class of transient motions investigated is the rise of bubbles undergoing a change of volume due to a decrease or increase of the ambient liquid pressure. In addition to drag, the volume change affects the added mass of the bubble and, therefore, the acceleration of its center of volume. In the case of an expanding bubble, the effect can be so strong as to actually cause the bubble to temporarily slow down before reaching the larger terminal velocity associated with the increased volume; conversely, for a contracting bubble, one may have a temporary acceleration.

The classic numerical simulations of the steady motion of bubbles under the action of a constant pressure gradient are due Ryskin and Leal who developed a method based on the use of orthogonal boundary fitted coordinates.[7–9]

We adopt here a refinement of this method based on our earlier work,[10] already used to study steady bubble rise in an axisymmetric shear flow,[11] and transient rise in a quiescent liquid.[12] Although the coordinate generation scheme is similar, the need to deal with bubbles with a variable volume has required some changes in the numerical algorithm.

II. MATHEMATICAL MODEL AND NUMERICAL METHOD

The mathematical model consists of the incompressible axisymmetric Navier–Stokes equations solved subject to the condition of vanishing tangential stress at the bubble surface and vanishing normal velocity gradient at infinity. The transients of concern in this paper are sufficiently slow that the gas pressure p inside the bubble can be considered spatially uniform and related to the instantaneous bubble volume $V(t)$ by the isothermal relation

$$p(t)V(t)=p_0V_0, \tag{1}$$

where p_0 and V_0 denote initial equilibrium values. At the

[a)]Also at: Department of Applied Physics, Twente Institute of Mechanics, and Burgerscentrum, University of Twente, AE 7500 Enschede, The Netherlands.

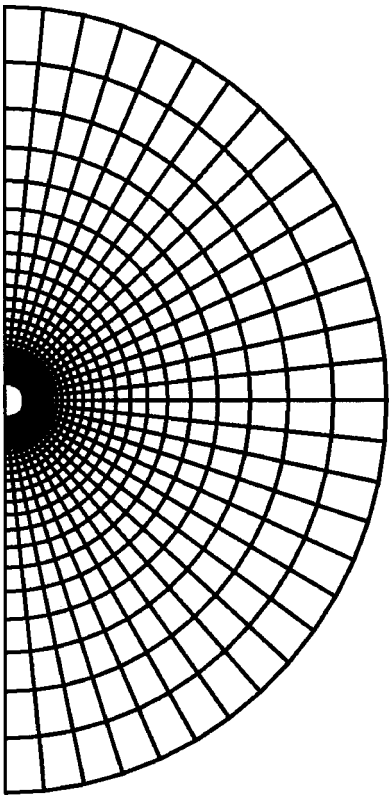

FIG. 1. An example of the computational grid.

bubble surface, the discontinuity in the normal stresses is balanced by the product of the (constant) surface tension coefficient and the local curvature.

In the numerical solution of the problem, in order to accurately account for the deforming shape of the bubble, we use boundary-fitted coordinates (ξ,η) related to cylindrical coordinates (r,x) by

$$\left[\frac{\partial}{\partial\xi}\left(f\frac{\partial}{\partial\xi}\right)+\frac{\partial}{\partial\eta}\left(\frac{1}{f}\frac{\partial}{\partial\eta}\right)\right]\begin{pmatrix}r\\x\end{pmatrix}=0, \tag{2}$$

in which $f=h_\eta/h_\xi$ is the distortion function defined by the ratio of the scale factors h_ξ and h_η in the ξ and η directions.[7,8] The trace of the bubble surface on the meridian plane corresponds to $\eta=1$. At each time step, the outer boundary, corresponding to $\eta=0$, is a sphere of radius S centered at the midpoint between the intersections of the bubble surface with the axis of symmetry. A regular grid of points is laid out in the computational domain and their image in the physical domain is found by solving (2). In this work, the function f is prescribed as

$$f=(\tfrac{3}{2}-\eta)M, \tag{3}$$

where M is the conformal module (see, e.g., Refs. 10, 13 and 14); this specification results in a refined grid near the bubble surface. An example of a grid generated in this way is shown in Fig. 1 and a detail near the bubble in Fig. 2.

The flow fields are calculated using the *SIMPLER* procedure (see, e.g., Refs. 15 and 16) on a standard staggered finite-difference grid arrangement with second-order accurate discretization except near the bubble boundary, where

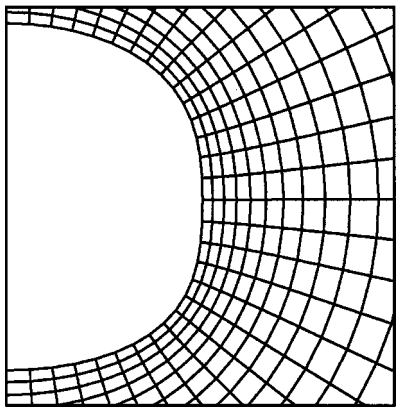

FIG. 2. Detail of the grid of the previous figure near the bubble.

the procedure is the following. Since this is a free-surface problem, the liquid velocity at the bubble surface must be found as part of the solution procedure. Here our procedure differs from that of Refs. 8, 9, and 11. The tangential velocity at the generic node (i,NJ) on the bubble surface is obtained from the condition of vanishing tangential stress

$$\frac{h_\xi}{h_\eta}\frac{\partial}{\partial\eta}\left(\frac{u_\xi}{h_\xi}\right)+\frac{h_\eta}{h_\xi}\frac{\partial}{\partial\xi}\left(\frac{u_\eta}{h_\eta}\right)=0, \tag{4}$$

which is discretized as (Fig. 3)

$$\frac{1}{3\Delta\eta}\left[8\left(\frac{u_\xi}{h_\xi}\right)_{i,NJ}-9\left(\frac{u_\xi}{h_\xi}\right)_{i,NJ-1/2}+\left(\frac{u_\xi}{h_\xi}\right)_{i,NJ-3/2}\right]$$
$$+\left(\frac{h_\eta}{h_\xi}\right)^2_{i,NJ}\frac{1}{\Delta\xi}\left[\left(\frac{u_\eta}{h_\eta}\right)_{i+1/2,NJ}-\left(\frac{u_\eta}{h_\eta}\right)_{i-1/2,NJ}\right]=0. \tag{5}$$

The three terms in the first square brackets are a one-sided, second-order accurate approximation to $(\partial/\partial\eta)(u_\xi/h_\xi)_{i,NJ}$. The mapping algorithm generates the values of the scale factors at points with integer labels; those at points with half-integer labels are obtained by averaging. This equation is

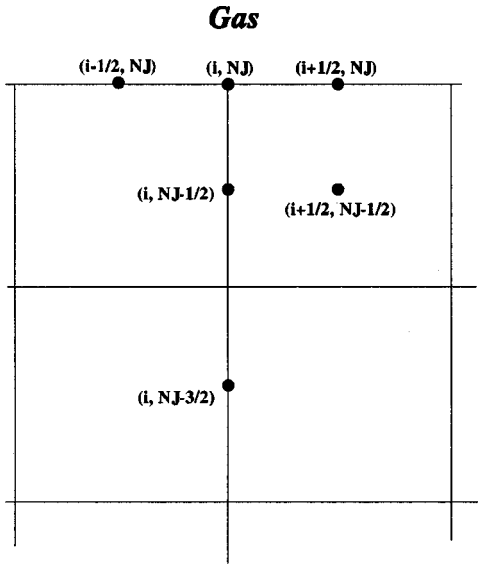

FIG. 3. Illustration of the discretization in Eq. (5).

solved for $(u_\xi)_{i,NJ}$ in terms of the most recent values of the velocities at neighboring points. After this step, a new estimate of the normal velocity $(u_\eta)_{i+1/2,NJ}$ is found by using the equation of continuity

$$\frac{1}{h_\xi h_\eta r}\left[\frac{\partial}{\partial\xi}(h_\eta r u_\xi)+\frac{\partial}{\partial\eta}(h_\xi r u_\eta)\right]=0, \tag{6}$$

discretized by central differences at $(i+1/2,NJ-1/2)$.

At each iteration, the *SIMPLER* method requires the solution of a Poisson equation for the pressure correction p' and, at the next step, for the pressure itself. At the bubble surface, the boundary condition associated with the pressure correction is simply $p'=0$, because there the velocity is found from (4) and (6) and therefore does not need to be updated. For the case of the pressure, on the other hand, we use a Dirichlet condition obtained from the normal stress condition evaluated at $i+1/2,NJ$

$$-p+2\mu\left(\frac{1}{h_\eta}\frac{\partial u_\eta}{\partial\eta}+\frac{u_\xi}{h_\xi h_\eta}\frac{\partial h_\eta}{\partial\xi}\right)$$
$$=-p(t)+\sigma\left[\frac{1}{h_\xi^3}\left(\frac{\partial x}{\partial\xi}\frac{\partial^2 r}{\partial\xi^2}-\frac{\partial^2 x}{\partial\xi^2}\frac{\partial r}{\partial\xi}\right)-\frac{1}{r h_\xi}\frac{\partial x}{\partial\xi}\right], \tag{7}$$

where the term in parentheses in the left-hand side is the (η,η) component of the rate of strain and the last term, multiplied by the surface tension coefficient σ, is the local curvature. On the outer boundary the normal velocity gradient is taken to vanish, while the pressure is taken to be hydrostatic.

At convergence of the iterative process, the nodes on the bubble surface are moved by the explicit first-order Euler method, and then interpolated by a cubic spline so as to generate a representation of the bubble surface at the new time level. At this point, a new boundary fitted grid is generated according to the procedure described in Ref. 10 and the new bubble volume is calculated for use in (1).

The generation of a new coordinate system at each time step has the effect that the grid points in physical space move in time. Thus, a special care is necessary in evaluating the convective derivatives in the momentum equations (see Ref. 12).

We have run tests with the radius S of the outer boundary equal to 20 and 30 times the initial bubble radius finding differences of the order of 0.2% in the terminal velocity; for $S=10$ times the initial radius, the error was of the order of 2%. For all the calculations reported here we used $S=20$. Convergence tests for the terminal velocity of an initially spherical 1 mm-radius bubble were run with 16×16, 32×32, and 48×48-node grids. The difference between the coarsest and the finest grid was of the order of 5%, while that between the intermediate and the finest grid was 0.3%. Orthogonality of the grid can be checked by monitoring the minimum over the nodes of the quantity

$$\cos\theta=\frac{1}{h_\xi h_\eta}(x_\xi x_\eta+y_\xi y_\eta), \tag{8}$$

which represents the angle between coordinate lines. With the 32×32 grid, the maximum difference $|90°-\theta|$ is about 4°, which can be reduced to 3° by increasing the number of nodes to 50×50 and, further, to 1° by going to an 80×80 grid.

TABLE I. Comparison of the present computational results with the measurements of Ref. 17.

Radius mm	Terminal velocity m/s		Aspect ratio	
	Experiment	Calculation	Experiment	Calculation
0.36	0.153±0.002	0.159	1.03	1.027
0.50	0.261±0.002	0.253	1.15	1.116
0.60	0.304±0.002	0.300	1.30	1.235

Some results obtained with the 32×32 grid and different bubble radii are compared in Table I with the data of Duineveld[17,18] who carried out measurements in ultrapure water. For an additional safety margin, in view of the transient nature of the motion and of the larger curvature of the bubble shape for some of the cases, the calculations reported here were obtained with a 50×50 (spherical and ellipsoidal shapes) or 60×60 (oval shapes) grid.

Since the present method is explicit, the time step has to be sufficiently small to resolve the fastest process included in the simulation. Because of surface tension, the shortest capillary waves on the bubble surface have a wavelength of the order of $2\pi R/N$, where N is the number of grid points along the surface. The corresponding period is of the order of $2\pi\sqrt{\rho R^3/\sigma N^3}$ which, with $R=0.6$ mm, $N=50$, $\rho=1000$ kg/m^3, $\sigma=0.0729$ J/m^2, gives 30.6 μs. Numerical tests showed that a time step of the order of 1/15 to 1/30 of this value gave converged results.

To validate the ability of the code to resolve time-dependent phenomena we have compared its predictions with several oscillations problems for which exact results exist. The first test is one in which the bubble executes isothermal spherically symmetric radial oscillations, a situation which can be described by means of the Rayleigh–Plesset

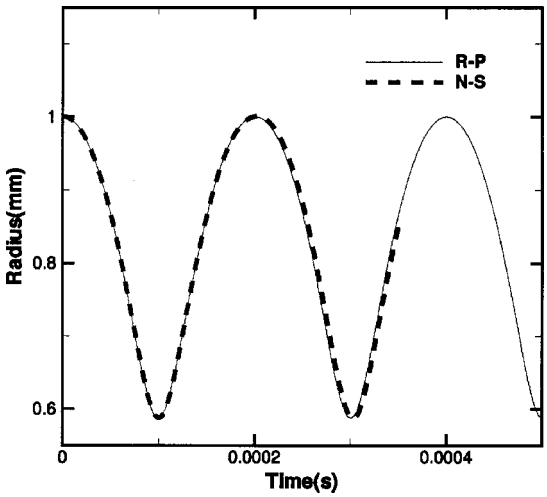

FIG. 4. Comparison between the results of the present method (dashed) and those from the Rayleigh–Plesset equation for the radial oscillations of an initially over-expanded spherical bubble.

FIG. 5. The four initial bubble shapes considered in this work: Sphere, prolate and oblate spheroids, and Cassini oval with $k=0.988$; the equivalent radius is the same in all four cases and is 0.6 mm.

FIG. 6. Left picture: Superposition of the terminal shapes for initially spherical and oval bubbles; right picture: Superposition of the terminal shapes for the initially ellipsoidal bubbles. In all cases the equivalent radius is 0.6 mm.

equation. Figure 4 compares the present results with the Rayleigh–Plesset calculation for an initial bubble radius of 1 mm, an initial internal pressure of 100 kPa, and an ambient pressure of 200 kPa. Note that the oscillation amplitude is relatively large and, accordingly, this represents a stringent test of the present calculation. These results were obtained with an 80×80 grid; a smaller 50×50 grid accurately reproduced the first period of oscillation, but gave an error of about 5% in the second period.

As a second test, we have calculated the period of the shape oscillations for the prolate-oblate mode for an initial aspect ratio $b/a=1.1$ with the linear-theory result (see, e.g., Ref. 19)

$$T_2^0=\pi\sqrt{\frac{\rho R_{\mathrm{eq}}^3}{3\sigma}}. \tag{9}$$

For $R=0.6$ mm, $\sigma=0.0729$ J/m^2, $\rho=1000$ kg/m^3 this equation gives 3.12 ms, while the numerical result with 80×80 and 50×50 grids is 3.23 and 3.35 ms, respectively. As a further test, we have repeated this calculation with $b/a=2$. It is known that the oscillation period lengthens as the amplitude increases. For the prolate-oblate mode, Ref. 20 gives the approximate result

$$\frac{T_2}{T_2^0}\simeq\left\{1-\frac{44\,893}{61\,740}\left[\frac{b/a-1}{1+b/2a}\right]^2\right\}^{-1}, \tag{10}$$

from which, for $b/a=2$, one finds a lengthening of 22%. Our numerical result, again for $R=0.6$ mm, is 3.65 ms with an 80×80 grid and 3.73 ms with a 60×60 grid; the difference with (10) is 2.5% and 4.3%, respectively.

The results of these tests suggest that the code works correctly and the spatial and temporal discretizations used are adequate.

III. SHAPE CHANGES

To explore the effect of the initial bubble shape on the terminal velocity we have used several initial shapes, all with the same equivalent radius R_0 (Fig. 5): A sphere of radius R_0, prolate and oblate spheroids with major and minor axes b and a, with $b/a=2$, and the solid obtained by rotating around the polar axis a Cassini oval, given by

$$\left(\frac{r^2+x^2}{a^2}+1\right)^2-4\frac{x^2}{a^2}=k^4. \tag{11}$$

If $k<1$, this curve consists of two disjointed ovals with foci at $\pm a$. As k approaches 1 from below, the ovals develop a larger and larger curvature until, for $k=1$, they join with a cusp at $x=0$ to form a lemniscate. This shape is chosen as the region of high curvature near the polar axis is qualitatively reminiscent of the shape of a bubble which has just pinched off from a needle.

The volume of the prolate spheroid is $V=\frac{4}{3}\pi a^2 b$, of the oblate spheroid $V=\frac{4}{3}\pi a b^2$, and of the Cassini oval

$$\frac{V}{a^3}=\frac{\pi}{2}\Bigg[\kappa_+(1+\kappa_+^2)-\kappa_-(1+\kappa_-^2)+\frac{\kappa^3}{2}\log\frac{2\kappa_++1+\kappa_+^2}{2\kappa_-+1+\kappa_-^2}-\frac{2}{3}\kappa_+(3+\kappa_+^2)+\frac{2}{3}\kappa_-(3+\kappa_-^2)\Bigg], \tag{12}$$

where $\kappa_\pm=\sqrt{1\pm k^2}$. The maximum curvature of the Cassini oval on the axis of symmetry is given by

$$a\mathcal{C}=\frac{2-k^2}{k^2\sqrt{1-k^2}}, \tag{13}$$

which gives $a\mathcal{C}=6.79$ for $k=0.988$.

Figure 6 shows the calculated terminal shapes of bubbles in water with an equivalent radius $R_0=0.6$ mm released with the four initial shapes mentioned before. Bubbles of this size were reported to rise rectilinearly in Ref. 2, and to exhibit different terminal velocities according to the manner of generation. The terminal shapes of the sphere and Cassini oval with $k=0.988$ are superposed in the left picture, and those of

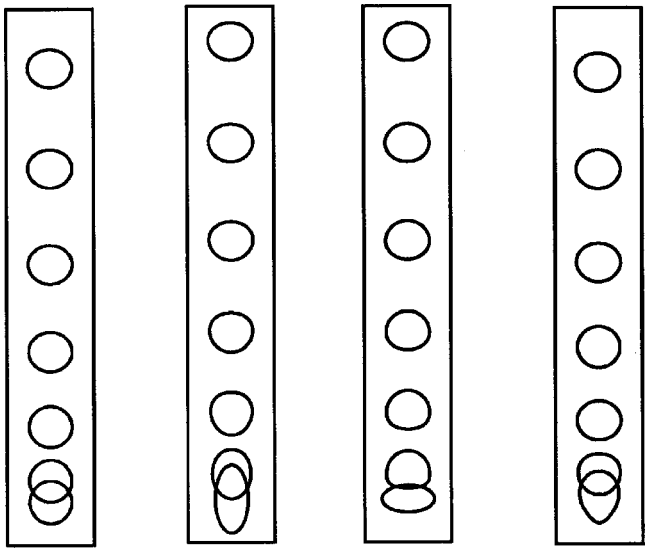

FIG. 7. Comparison of shape and position of the four bubbles of Fig. 5 at 10 ms-intervals.

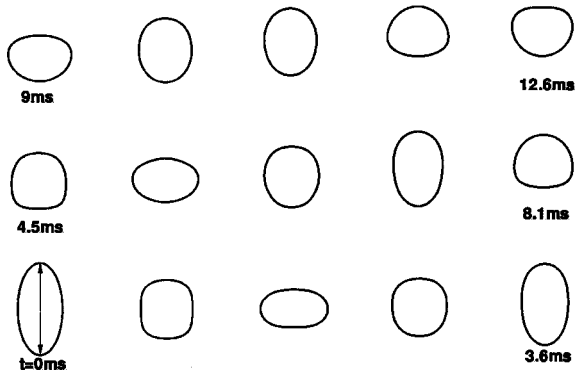

FIG. 8. Successive shapes at 0.9 ms intervals of the initially prolate-spheroidal bubble; the equivalent radius is 0.6 mm; the arrow has a length of 1.905 mm. In each row, the bubble vertical position is relative to the shape at the beginning of the row.

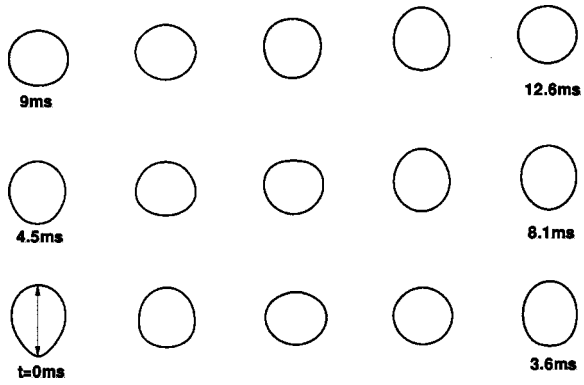

FIG. 10. Successive shapes at 0.9 ms intervals of the initially oval bubble; the equivalent radius is 0.6 mm and $k=0.988$; the arrow has a length of 1.447 mm. In each row, the bubble vertical position is relative to the shape at the beginning of the row.

the two spheroids in the right picture. The shapes are barely distinguishable from each other, with any small difference imputable to numerical error.

We define the rise velocity of the bubble as the velocity of its center of volume x_V given by

$$x_V=\frac{1}{V}\int_{x_0}^{x_1} x\pi r^2(x)dx, \tag{14}$$

where the bubble extends in the range $x_0\leqslant x\leqslant x_1$ and $r(x)$ is the distance of the surface element from the axis of symmetry (this formula is modified in an obvious way in regions of the bubble surface which are convex toward the liquid). The terminal velocities computed in the four cases are very close: 0.300 m/s for the spherical, prolate, and oblate shapes, and 0.298 m/s for the Cassini oval.

These results suggest that, contrary to observations reported in Refs. 2 and 4, there is no significant difference among the four results. Figure 7 shows side by side the four bubbles at 10 ms-intervals. The difference in the distances travelled at equal times are a consequence of the shape oscillations that take place in the different cases, as will be further discussed below.

Figures 8–10 are a more detailed illustration of the successive shapes of the three initially nonspherical bubbles during the early stages of the process. The amplitude of the surface-tension-driven shape oscillations of the spheroidal cases are greater than for the Cassini oval in view of their greater initial surface energy (Table II). The period, measured from a Fourier transform of the computed aspect ratios (defined as the ratio of the length of the bubble along the axis of symmetry to its maximum width), is 3.39, 3.39, and 3.77 ms, respectively, for the prolate, oblate, and Cassini oval shapes. The presence of a second harmonic at 1.69 and 1.75 ms was clear for the prolate and oblate cases, respectively, but was less well defined for the oval case in which many surface modes are simultaneously present. In all cases, the bubble volume changed by less than 0.1% with respect to the initial value.

A comparison of the rise velocities of the spherical, prolate, and oblate bubbles is shown in Fig. 11. The velocity of the ellipsoidal bubbles is not monotonic due to the strong shape oscillations, and, as expected, the oscillations of the prolate and oblate bubbles have opposite phases. It is interesting to note that the difference between the maxima and the spherical bubble velocity is greater than that of the minima. This fact is due to the very strong effect of bubble deformation on its drag and added mass (see, e.g., Ref. 21), and is further illustrated in Fig. 12, which shows both the instantaneous rise velocity and aspect ratio for the initially prolate bubble. A very similar result is found in the initially oblate case. The distance travelled by the two spheroidal bubbles is the same.

A comparison of the spherical case with the $k=0.988$ Cassini oval is shown in Fig. 13. The situation is qualitatively very similar to that depicted in Fig. 11, except that, due to the smaller amplitude of the shape oscillations, the

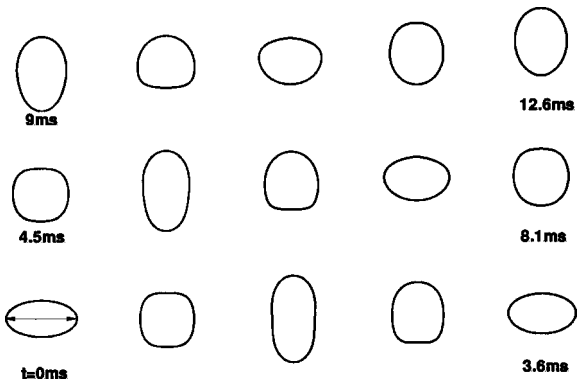

FIG. 9. Successive shapes at 0.9 ms intervals of the initially oblate-spheroidal bubble; the equivalent radius is 0.6 mm; the arrow has a length of 1.512 mm. In each row, the bubble vertical position is relative to the shape at the beginning of the row.

TABLE II. Nondimensional surface area of the shapes of Fig. 5 in excess of that of a sphere of equal volume.

Shape	Excess surf. area/$4\pi R_0^2$
Prolate	0.077
Oblate	0.096
Cassini oval ($k=0.988$)	0.012

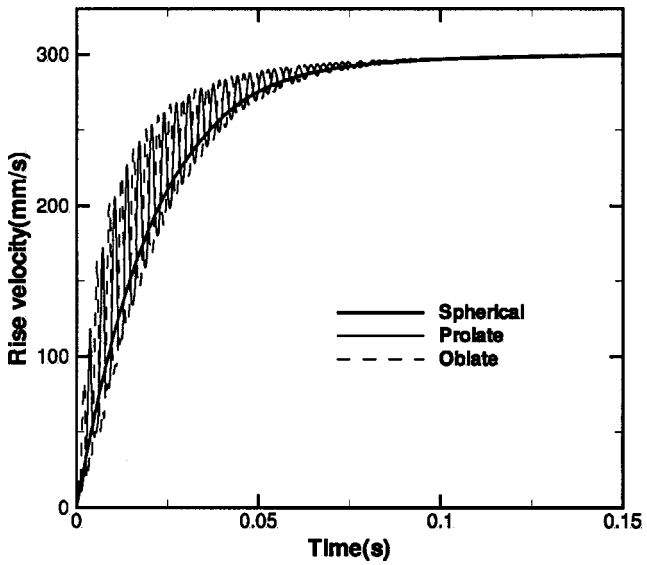

FIG. 11. Rise velocities of the spherical (thick solid line), prolate (thin solid line), and oblate (dashed line) bubbles vs time.

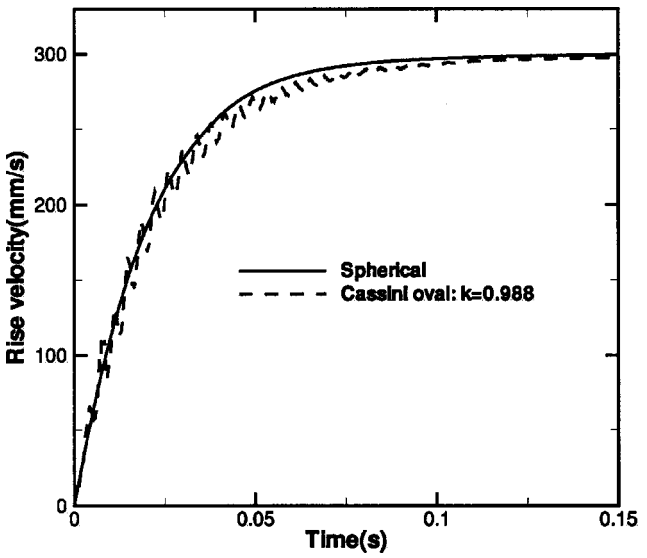

FIG. 13. Rise velocities of the spherical (thick solid line) and $k=0.988$ oval bubbles vs time.

differences with the spherical case are smaller. The terminal velocities are indistinguishable within the present accuracy.

IV. VOLUME CHANGES

We now turn to a different problem, in which the bubble undergoes a volume change in the course of its ascent in response to the time variation of the ambient pressure, which we take to be given by

$$P_\infty(t)=P_0\pm\frac{1}{2}\Delta p\left[1-\tanh\left(\frac{t-t_0}{\tau}\right)\right], \tag{15}$$

with the upper sign corresponding to a pressure decrease from $P_0+\Delta p$ to P_0 and the lower sign to a pressure increase from $P_0-\Delta p$ to P_0. The interest of this situation lies in the dependence of the bubble added mass on its volume. Furthermore, the rapid change in buoyancy leads to an accelerated motion which is useful to illuminate the role of the memory force.

For a spherical bubble with instantaneous radius $R(t)$ in buoyant rise with a velocity $U(t)$ in a quiescent liquid, with the neglect of the memory force, one may write an approximate equation of motion in the form

$$\frac{d}{dt}\left(\frac{2}{3}\pi\rho R^3U\right)=\frac{4}{3}\pi R^3\rho g-\frac{1}{2}\pi R^2\rho C_D|U|U, \tag{16}$$

where g is the acceleration of gravity and C_D is the drag coefficient. Equation (16) may be recast in the equivalent form

$$\frac{dU}{dt}=-\frac{3}{R}\frac{dR}{dt}U+2g-\frac{3}{4}\frac{C_D}{R}|U|U, \tag{17}$$

from the first term in the right-hand side of which the effect of the volume change on the rise velocity is apparent.[22,23]

For a small bubble, the terminal velocity scales like $U\propto R^2g/\nu$, where ν is the liquid kinematic viscosity. This relation can be explicitly verified when the drag force can be estimated from either the Hadamard–Rybczynsky or Levich relations. The velocity of larger bubbles, chiefly dependent on form rather than viscous drag, scales instead like $\sqrt{gR}$. In either case, one finds $\Delta U/U\sim\Delta R/R$, which shows that the left hand side and the first term in the right-hand side of (17) are in all cases comparable in magnitude.

When the radial inertia of the bubble is small, from (1) one has the estimate $\Delta R/R\sim\Delta P_\infty/P_\infty$. Therefore, the first term in the right-hand side of (17) is negligible compared to the second one when $\Delta P_\infty/P_\infty\ll g\tau/U$, in which τ is the time scale for the ambient pressure variation. For small bubbles this gives $\Delta P_\infty/P_\infty\ll\nu\tau/R^2$. For millimeter-size bubbles, with $\nu\sim10^{-6}$ m^2/s, this estimate gives $\Delta P_\infty/P_\infty\ll\nu$ (ν in m^2/s). For larger bubbles, for which $U\sim\sqrt{gR}$, we find instead $\Delta P_\infty/P_\infty\ll0.1\tau$ (τ in seconds). Both conditions

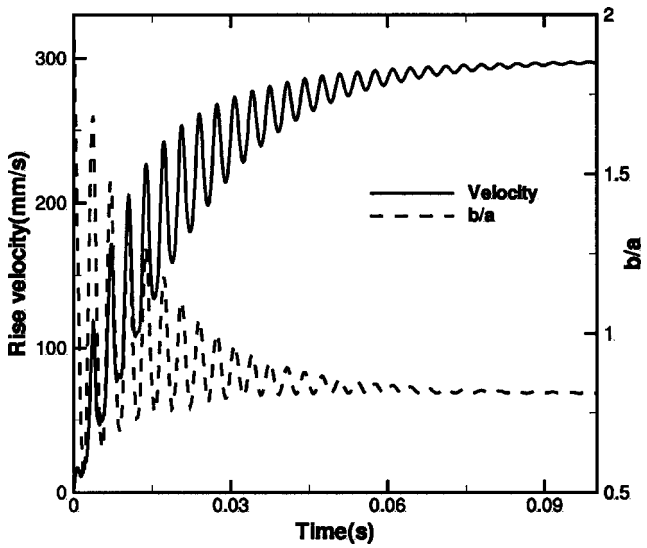

FIG. 12. Rise velocity (solid line) and aspect ratio vs time during the rise of an initially prolate bubble with initial aspect ratio $b/a=2$.

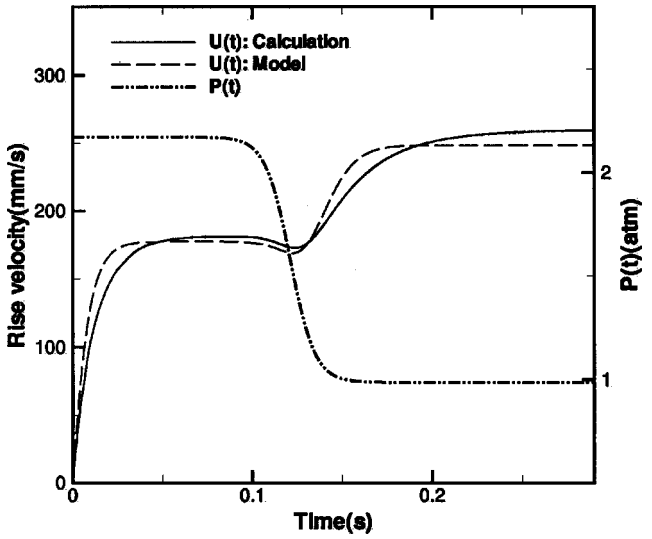

FIG. 14. Rise velocity of a bubble with an initial radius $R(0)=0.4$ mm when the ambient pressure (shown by the dash–dot line, right vertical scale) falls from 220 to 100 kPa. The dashed line is the result from the simplified model of Eq. (17) not including the memory force.

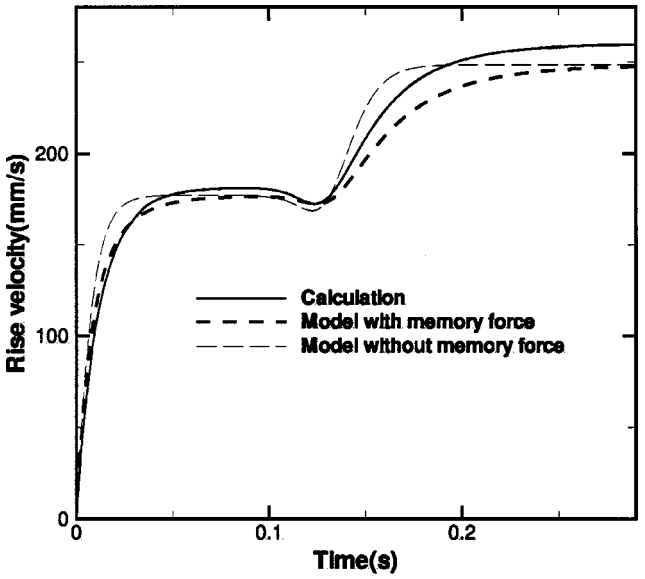

FIG. 15. The rise velocity of the expanding bubble of the previous figure as computed with the present numerical method (solid line) compared with the simple model of Eq. (17), without memory force (long dashes), and with the model of Eq. (20), with memory force.

will only be verified for slow or relatively minor pressure changes, which shows that the effect of present concern can readily occur in practical situations.

In order to impose the ambient pressure boundary condition, in the numerical computation for this case, it proves convenient to maintain the pressure at infinity at the reference value adding (15) to the right-hand side of (7). The bubble shape in the cases simulated here remains essentially spherical, so that the grid is little distorted. We have used grids with 60×60 nodes for the examples that follow.

The solid line in Fig. 14 shows results for the rise velocity of a bubble with an initial radius $R(0)=0.4$ mm with an ambient initial pressure of 220 kPa when, in (15), one takes $P_0=100$ kPa, $\Delta p=120$ kPa, $t_0=120$ ms, $\tau=13.77$ ms. The bubble is released from rest with a spherical shape; its velocity gradually increases and reaches a terminal value of 0.181 m/s. Until this point the ambient pressure, shown by the dash–dot line, has changed very little. When the pressure starts falling, at first the bubble slows down and then, as its radius reaches its terminal value and the pressure stabilizes, accelerates again reaching the terminal velocity of 0.266 m/s corresponding to the final equilibrium radius of 0.5224 mm. This behavior is quite clear in the light of Eqs. (16) or (17): When there is a rapid time dependence, the left-hand side of (16) dominates and shows that $R^3U\sim$constant, which corresponds to a conservation of the impulse: a radius increase forces therefore a decrease of U. When steady conditions are reached, the left-hand side of (16) is negligible, and the rise velocity settles to the value appropriate for the increased volume.

The dashed line in Fig. 14 is found by integrating Eq. (17) with C_D given by[24]

$$C_D=\frac{48}{\mathrm{Re}}G(\chi)\left(1+\frac{H(\chi)}{\sqrt{\mathrm{Re}}}\right), \tag{18}$$

where

$$\mathrm{Re}=\frac{2R(t)U}{\upsilon}. \tag{19}$$

χ is the aspect ratio, evaluated from Eq. (1.5) of Ref. 24, $G(\chi)$ is given by Eq. (2.12) there, and $H(\chi)$ is obtained by interpolation from the data in Table I of the same reference. While the result found from the simplified model is qualitatively similar to the more accurate one, a substantial quantitative difference remains which, as one reviewer remarked, is somewhat puzzling. For example, for small times, there is nearly a factor of 2 difference in the acceleration, in spite of the fact that the flow is nearly potential so that buoyancy would be expected to dominate.

In trying to address this question we have considered whether the origin of the discrepancy could be traced to the neglect of the memory force, with the inclusion of which Eq. (16) would take the form

$$\frac{d}{dt}\left(\frac{2}{3}\pi\rho R^3U\right)=\frac{4}{3}\pi R^3\rho g-\frac{1}{2}\pi R^2\rho C_D|U|U - \int_0^t G(t-\tau)\frac{dU}{d\tau}d\tau, \tag{20}$$

where G is an appropriate kernel. For a spherical bubble of constant radius at small Reynolds number, Yang and Leal[25] (see also Refs. 23, 26, and 27) give

$$G(t)=8\pi\mu R\exp\left(\frac{9\upsilon t}{R^2}\right)\mathrm{erfc}\left(3\sqrt{\frac{\upsilon t}{R^2}}\right). \tag{21}$$

In Fig. 15 we compare the fully numerical solution (solid line) with the solution of (20) (dotted line); the dashed line is the solution of (16), already shown in Fig. 14, which does not include the memory force. The correction is in the right direction in that Eq. (20) better approximates the Navier–Stokes solution. A good part of the residual difference is due

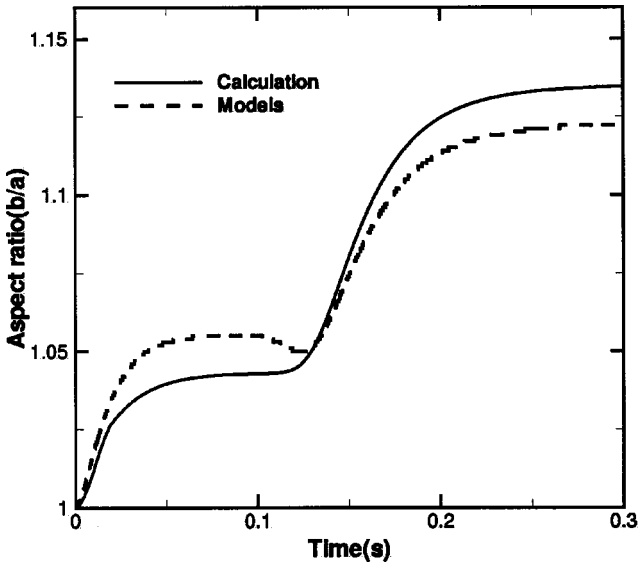

FIG. 16. Calculated aspect ratio vs time for the expanding bubble of the previous two figures (solid line) compared with the results predicted for the same instantaneous velocity by the theories of Refs. 24 and 28 (dashed line).

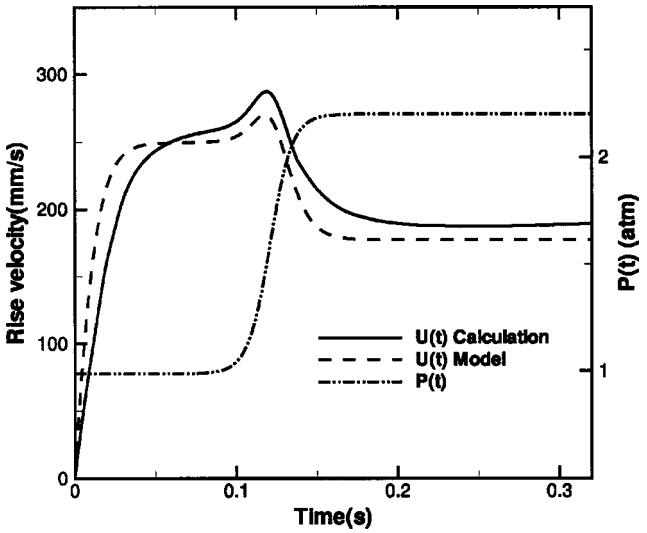

FIG. 17. Rise velocity of a bubble with an initial radius $R(0) = 0.5224$ mm when the ambient pressure (shown by the dash–dot line, right vertical scale) rises from 100 to 220 kPa. The dashed line is the result from the simplified model of Eq. (17) without the memory force.

to the fact that (18) over-estimates the drag coefficient by about 5%. In order to investigate whether this difference is due to an incorrect estimation of the aspect ratio χ, we compare in Fig. 16 the aspect ratio as computed from the present Navier–Stokes simulation (solid line) with the theoretical results of Refs. 24 and 28 (see also Ref. 29), which essentially coincide for the velocities encountered here. To isolate the effect of the aspect ratio modeling, we used the instantaneous translational velocity calculated from the full Navier–Stokes solution. The models exhibit some difference from the numerical results which, however, is able to account only for about half of the difference in terminal velocities. The remainder is likely due to higher-order Reynolds-number terms not included in (18).

In spite of its apparently good performance, it should be noted that the model used for the memory force in (21) is really applied outside its expected range of validity. Even in the early stages of the process, when both the bubble radius and rise velocity are small, the Reynolds number is about 50–100, rather than small. Secondly, as shown by Magnaudet and Legendre,[30] the argument t/R^2 in (21) should be replaced by $\int dt/R^2$ for a variable radius.

The solid line in Fig. 17 shows the rise velocity of a bubble undergoing a contraction from a radius equal to the terminal radius of the previous case, $R(0) = 0.5224$ mm, to the initial radius of the previous case, 0.4 mm, under the action of an increasing ambient pressure, given by (15) with the lower sign and $P_0 = 220$ kPa, $\Delta p = 120$ kPa, $t_0 = 120$ ms, $\tau = 13.77$ ms $R(0) = 0.5224$ mm; the dashed line is the simple model (17). Now impulse conservation has the effect of causing an increase of the rise velocity before it settles down to the smaller value associated with the reduced radius. The addition of the memory force (Fig. 18) improves somewhat the simplified model, but not as much as in the previous case.

A recent paper[31] reports experimental observations on the rise velocity of expanding and contracting bubbles. Qualitatively the results are the same as found here. Unfortunately, no quantitative comparison is possible as the water used in the experiment was contaminated with surface-active agents which had a strong impact on the terminal velocities of the bubbles.

V. CONCLUSIONS

In the present paper we have applied an accurate boundary fitted numerical method to the calculation of the rise velocity of bubbles undergoing shape or volume oscillations.

We have found that the shape with which the bubble is released, and the oscillations through which it relaxes to the

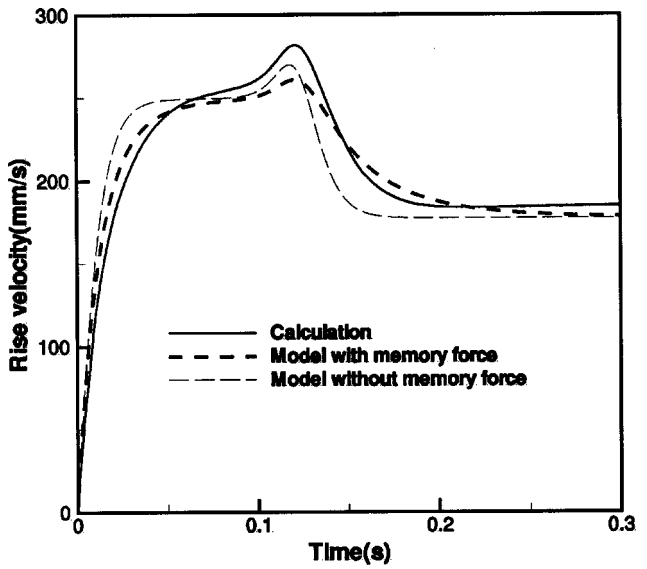

FIG. 18. The rise velocity of the contracting bubble of the previous figure as computed with the present numerical method (solid line) compared with the simple model of Eq. (17), without memory force (long dashes), and with the model of Eq. (20), with memory force.

final steady shape, do not affect the calculated terminal velocity or shape. This finding is contrary to recently reported experimental results. If the solution of the problem is indeed nonunique, as suggested by these results, one might conjecture that, in the parameter space of the problem, we have chosen initial conditions all belonging to the ''domain of attraction'' of the same terminal shape. While this explanation cannot be ruled out, the ease with which the effect is observable in experiment would seem to make it rather unlikely. The other possibility is that, in spite of the considerable care taken by the experimenters, some residual surface contamination was present, perhaps due to slightly soluble surfactants in the fluid line where the bubble is generated. If this is so, the observed difference in terminal velocities might perhaps be due to the effect of the initial oscillations on the surface impurities: a bubble released from a small-bore needle executes strong surface oscillations which might perhaps lead to the shedding of surface contaminants.[2] The bubble would then rise faster, as observed, and, since the liquid is very clean, it would not pick up further contaminants. It is disturbing that such a fundamental issue still appears to be unresolved after so many decades of study of such an apparently simple fluid dynamical phenomenon.

In the second part of the paper, we have studied bubbles rising in a time-dependent ambient pressure environment. The changing pressure affects the bubble radius and, as a consequence, both the impulse and the buoyant force on the bubble. While the tendency to conserve impulse tends to cause a slowing down of an expanding bubble and an acceleration of a contracting bubble, buoyancy is stronger on a bigger bubble and weaker on a smaller one so that the two effects counter each other during the transient.

ACKNOWLEDGMENTS

We thank a reviewer for suggesting that the difference of Fig. 14 between the exact result and the simplified model might be due to the memory force; Figs. 15 and 18 are the result of investigating this suggestion. The work of the first two authors has been supported by NASA under Grant No. NAG3-2362. S.T. acknowledges support by the Japan Ministry of Education.

[1] M. Wu, E. Englert, and M. Gharib, ''Contamination is not the only way to slow down rising air bubbles,'' Bull. Am. Phys. Soc. **45**, 31 (2000).
[2] M. Wu and M. Gharib, ''Experimental studies on the shape and path of small air bubbles rising in clean water,'' Phys. Fluids **14**, L49 (2002).
[3] A. Tomiyama, Y. Nakahara and G. Morita, ''Rising velocities and shapes of single bubbles in vertical pipes,'' in 4th International Conference on Multiphase Flow, edited by E. Michaelides, Paper No. 492 (2001).
[4] A. Tomiyama, G. P. Celata, S. Hosokawa, and S. Yoshida, ''Terminal velocity of single bubbles in surface tension force dominant regime,'' Int. J. Multiphase Flow **28**, 1497 (2002).
[5] R. C. Clift, J. R. Grace, and M. E. Weber, *Bubbles, Drops, and Particles* (Academic, New York, 1978).
[6] D. Bhaga and M. E. Weber, ''Bubbles in viscous liquids: Shapes, wakes and velocities,'' J. Fluid Mech. **105**, 61 (1981).
[7] G. Ryskin and L. G. Leal, ''Orthogonal mapping in two dimensions,'' J. Comput. Phys. **98**, 254 (1983).
[8] G. Ryskin and L. G. Leal, ''Numerical solution of free-boundary problems in fluid mechanics. Part I. The finite-difference technique,'' J. Fluid Mech. **148**, 1 (1984).
[9] G. Ryskin and L. G. Leal, ''Numerical solution of free-boundary problems in fluid mechanics. Part II. Buoyancy-driven motion of a gas bubble through a quiescent liquid,'' J. Fluid Mech. **148**, 19 (1984).
[10] R. Duraiswami and A. Prosperetti, ''Orthogonal mapping in two dimensions,'' J. Comput. Phys. **98**, 254 (1992).
[11] S. Takagi, A. Prosperetti, and Y. Matsumoto, ''Drag coefficient of a gas bubble in an axisymmetric shear flow,'' Phys. Fluids **6**, 3186 (1994).
[12] S. Takagi, Y. Matsumoto, and H. Huang, ''Numerical analysis of a single rising bubble using boundary-fitted coordinate system,'' JSME Int. J. **B40**, 42 (1997).
[13] L. V. Ahlfors, *Lectures on Quasiconformal Mappings* (Van Nostrand, Princeton, 1966).
[14] O. Lehto and K. I. Virtaanen, *Quasiconformal Mappings in the Plane* (Springer, Berlin, 1973).
[15] C. A. J. Fletcher, *Computational Techniques for Fluid Dynamics* (Springer, Berlin, 1988).
[16] J. H. Ferziger and M. Periç, *Computational Methods for Fluid Dynamics*, 3rd ed. (Springer, Berlin, 2002).
[17] P. C. Duineveld, ''Bouncing and coalescing of two bubbles in water,'' Ph.D. thesis, University of Twente, The Netherlands (1994).
[18] P. C. Duineveld, ''The rise velocity and shape of bubbles in pure water at high Reynolds number,'' J. Fluid Mech. **292**, 325 (1995).
[19] H. Lamb, *Hydrodynamics*, 6th ed. (Cambridge University Press, Cambridge, 1932).
[20] J. A. Tsamopoulos and R. A. Brown, ''Nonlinear oscillations of inviscid drops and bubbles,'' J. Fluid Mech. **127**, 519 (1983).
[21] D. W. Moore, ''The boundary layer on a spherical gas bubble,'' J. Fluid Mech. **16**, 161 (1963).
[22] D. Lhuillier, ''Forces d'inertie sur une bulle en expansion se dèplaçant dans un fluide,'' C.R. Acad. Sci. Paris Série II **295**, 95 (1982).
[23] J. Magnaudet and I. Eames, ''The motion of high-Reynolds-number bubbles in inhomogeneous flows,'' Annu. Rev. Fluid Mech. **32**, 659 (2000).
[24] D. W. Moore, ''The velocity of rise of distorted gas bubbles in a liquid of small viscosity,'' J. Fluid Mech. **23**, 749 (1965).
[25] S. M. Yang and L. G. Leal, ''A note on the memory-integral contributions to the force on an accelerating spherical drop at low Reynolds number,'' Phys. Fluids A **3**, 1822 (1991).
[26] P. M. Lovalenti and J. F. Brady, ''The force on a bubble, drop, or particle in arbitrary time-dependent motion at small Reynolds number,'' Phys. Fluids A **5**, 2104 (1993).
[27] V. Galindo and G. Gerbeth, ''A note on the force on an accelerating spherical drop at low-Reynolds number,'' Phys. Fluids A **5**, 3290 (1993).
[28] T. B. Benjamin, ''Hamiltonian theory for motions of bubbles in an infinite liquid,'' J. Fluid Mech. **181**, 349 (1987).
[29] J. F. Harper, ''A bubble rising in viscous fluid: Lagrange's equations for motion at a high Reynolds number,'' in *IUTAM Sympsoium on Free Surface Flows*, edited by A. C. King and Y. D. Shikmurzaev (Kluwer, Dordrecht, 2001), pp. 107–111.
[30] J. Magnaudet and D. Legendre, ''The viscous drag on a spherical bubble with a time-dependent radius,'' Phys. Fluids **10**, 550 (1998).
[31] C. D. Ohl, A. Tijink, and A. Prosperetti, ''The added mass of an expanding bubble,'' J. Fluid Mech. **482**, 271 (2003).